Chemistry Europe
European Chemical Societies Publishing

WILEY VCH

Excellence in Chemistry Research

Announcing our new flagship journal

- Gold Open Access
- Publishing charges waived
- Preprints welcome
- Edited by active scientists

Meet the Editors of *ChemistryEurope*

Luisa De Cola
Università degli Studi di Milano Statale, Italy

Ive Hermans
University of Wisconsin-Madison, USA

Ken Tanaka
Tokyo Institute of Technology, Japan

ChemistrySelect

Research Article
doi.org/10.1002/slct.202200302

Chemistry Europe
European Chemical Societies Publishing

www.chemistryselect.org

Selective Catalytic Reduction of NOx with NH_3 over Mn_2O_3 Supported with Different Morphology of CeO_2 Catalysts

Shyam Sunder Rao, Vivek Kumar Patel, and Sweta Sharma*[a]

Three different morphologies of CeO_2 supports (nanoparticle, nanocube, and nanorod) were prepared by hydrothermal technique and further Mn_2O_3 metal was impregnated on CeO_2 supports using wet-impregnation methods, and their activity for NO reduction using NH_3–SCR technique was analysed. The synthesized catalysts and supports were further characterized through scanning electron microscopy (SEM), Energy-dispersive X-ray spectroscopy (EDX), X-ray diffraction (XRD), X-ray Photoelectron Spectroscopy (XPS), and transmission electron microscopy (TEM), and Brunauer-Emmett-Teller (BET). The catalytic performance of Mn_2O_3/CeO_2-nanoparticle has shown the highest conversion (76%) compared to the other two catalysts in the temperature range of 50–450 °C.

Introduction

The exponential growth of population and industrialization led to the emission of various pollutants in the environment, causes adverse effects on our environment and subsequently leading to climate change. Nitrogen oxides (NO_x), one of the major air pollutants, emitted from mobile and stationary sources cause genuine environmental issues, such as photochemical smog, acid rain, ozone depletion, and greenhouse effects.[1,2] At present, various strict environmental legislations are being implemented worldwide to reduce the concentration of NO_x before releasing it into the environment.[3,4] There are many techniques, such as non-selective catalytic reduction (NSCR),[5] selective catalytic reduction (SCR),[6,7] photocatalytic[8,9] etc., among which SCR technique using NH_3 as the reducing agent has been commercially applied in stationary source combustion units that require a higher removal efficiency of NO_x than NSCR, photocatalytic or combustion controls. In this process, NO_x emissions are converted into water vapors and nitrogen gas molecules which is V_2O_5–WO_3/TiO_2 based catalysts are widely used in NH_3–SCR due to their cost effectiveness, best de-nitration efficiency, good sulfur resistance within a temperature range of 300–400°C.[10,11] Though, there are certain disadvantages of vanadium-based catalysts such as its narrow temperature window, the high toxicity of V_2O_5, high oxidation activity towards SO_2 converted into SO_3 and N_2O production at higher temperatures.[12,13,14] The gases exhausted from stationary sources, for example, steel, cement, and glass plants are in a temperature range of 100–300 °C.[15,16] Therefore, extra energy is needed to heat the exhaust gasses to give good performance by NH_3–SCR catalysts.[17,18] Therefore, there is a need to develop a suitable catalyst whose performance should be high at the low-temperature range of 100–300 °C.

CeO_2 has received a lot of attention because of its excellent redox characteristics and strong oxygen mobility about oxygen vacancies.[19,20] Mn-based catalysts have been also thoroughly explored for the reduction of NO_x by NH_3–SCR in the last few years due to their excellent low-temperature catalytic activity.[21,22,23] As a result, the addition of CeO_2 to MnO_x–based catalysts may boost catalytic performance in the reduction of NO_x. It has been observed that MnO_x–CeO_2 catalysts, among the many bimetallic oxides, have a lot of potential owing to the high oxygen storage capacity of CeO_2.[24,25] In addition, other properties such as morphology and microstructure of catalysts also influence the catalytic activity and selectivity by changing active site pore structure and dispersion.[26,27] The enhancement of catalytic activity in NO reduction has been validated by several works. Li et al. synthesized CeO_2–MnO_x catalyst with a core-shell structure and tested for NO reduction by NH_3–SCR exhibited high conversion of NO in the temperature range of 110–220 °C range due to high concentrations of Mn^{4+} and Ce^{3+} and good resistance to SO_2 and H_2O.[28] Liu and labmates[29] synthesized MnO_x-CeO_2 shell-in-shell microsphere structure catalyst using hydrothermal method. The result showed high NO_x conversion by NH_3–SCR at low temperatures (lower than 210 °C), compared to catalyst synthesized by the co-precipitation method. Chao et al. found that MnO_x-CeO_2-Al_2O_3 catalysts showed high NO_x conversion and strong redox ability at low temperatures.[24] Li et al. synthesized mesoporous MnO_x–CeO_2 composites,[30] which gave better performance for NO_x conversion as well as exhibited significant resistance to SO_2 and H_2O.

In the present work, a series of supported Mn_2O_3/CeO_2 with different ceria morphologies were successfully synthesized to study the support morphology influence on metal-support interaction.

[a] S. Sunder Rao, V. Kumar Patel, S. Sharma
Department of chemical engineering,
Indian Institute of Technology (Banaras Hindu University)
Varanasi, 221005, India
E-mail: shweta.che@itbhu.ac.in

Supporting information for this article is available on the WWW under https://doi.org/10.1002/slct.202200302

Results and discussion

Physicochemical Characterization

XRD

The XRD pattern of CeO_2–NR, CeO_2–NP, CeO_2–NC, Mn_2O_3, Mn_2O_3/CeO_2–NR, Mn_2O_3/CeO_2–NC, and Mn_2O_3/CeO_2–NP are shown in Figure 1. The diffraction peaks observed at 28.36° 32.70°, 47.13°, 55.90°, 58.73°, 69.15°, 76.41° and 78.76° corresponding to (111), (200), (220), (311), (222), (400), (331) and (420) crystal plane of ceria respectively and it is cubic face-centered (a = b = c = 5.412 Å) (JCPDS 81,0792). In the case of Mn_2O_3, the diffraction peaks at 23.10°, 32.91°, 38.22°, 45.09°, 49.29°, 55.12°, and 65.80° corresponding to (211), (222), (400), (332), (431), (440), and (622) crystal planes respectively were observed, and it showed cubic body-centered type crystal structures (a = b = c = 9.420 Å) (JCPDS 89, 2809). [2,10] It indicated that all samples are crystalline. The Scherrer equation calculates the average crystal size of supports and catalysts and is summarized in Table 1. CeO_2–NP showing the smallest crystal size, whereas CeO_2–NR has the largest. The orders of crystal size of CeO_2 morphology are as follows: CeO_2–NP > CeO_2–NC > CeO_2–NR.

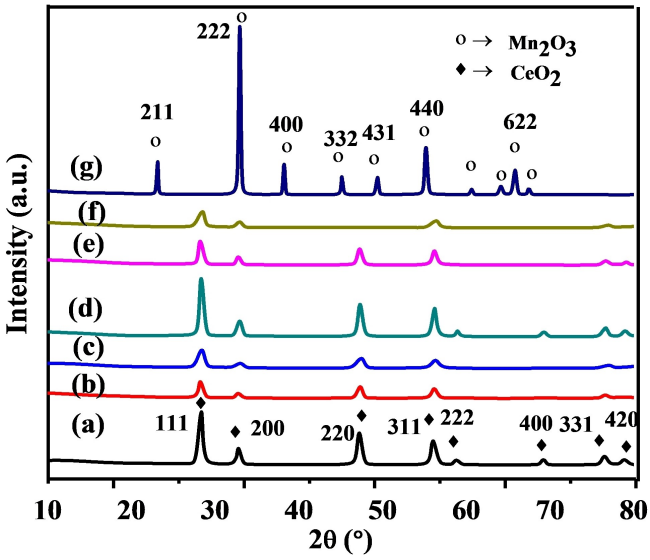

Figure 1. XRD pattern of catalysts (a) CeO_2–NR, (b) CeO_2–NC (c), CeO_2–NP, (d) Mn_2O_3/CeO_2–NR, (e) Mn_2O_3/CeO_2–NC (f), Mn_2O_3/CeO_2–NP, and (g) Mn_2O_3.

Table 1. Average crystal size and particles size of CeO_2 supports and Mn_2O_3/CeO_2 catalysts.

Sample	Average crystal size (nm)	Average particle size (nm)
CeO_2–NP	7.4	11
CeO_2–NC	11.2	37.5
CeO_2–NR	12.2	63
Mn_2O_3/CeO_2–NP	8.3	26
Mn_2O_3/CeO_2–NC	12.4	85
Mn_2O_3/CeO_2–NR	13.0	82

The impregnation of Mn_2O_3 over improved the crystal size of all the catalysts. It may be due to the shared cubic structure of Mn_2O_3 with ceria morphology. There are no diffraction peaks observed related to Mn_2O_3 in all the samples, showing that Mn_2O_3 is highly dispersed over the CeO_2 supports.[10,13]

BET

The specific surface area, pore size, and pore volume of the Mn_2O_3 impregnated on different CeO_2 morphology are listed in Table 2. The specific surface area of Mn_2O_3/CeO_2–NR, Mn_2O_3/CeO_2–NC, and Mn_2O_3/CeO_2–NP are 22.69, 30.45, and 34.53 m^2/g, respectively. Mn_2O_3/CeO_2–NP shows the highest specific surface area and pore volume compared to the other two catalysts, which should be ascribed to the strong interaction between Mn_2O_3 and CeO_2–NP or due to its lower crystalline nature, as also evident by XRD. The BET surface area samples were decreased may be due to the blocking effect on pores arising from the impregnation of Mn_2O_3 to CeO_2 species.

XPS

The elements that exist within a material (elemental composition) covering its surface and oxidation states in the material were identified using X-ray photoelectron spectroscopy (XPS), with the spectrum of this study shown in Figure 2.

The Ce 3d spectra of the catalysts are shown in Figure 2(a). All catalysts were de-convoluted into six peaks, which were represented as u^o, u^i, u^{ii}, v^o, v^i, and v^{ii}. The spin-orbit doublet peak's series represented by u and v respectively denote the Ce 3d3/2, and Ce 3d5/2 states. According to analyzed catalysts, it was found that both Ce^{3+} and Ce^{4+} ions are dispersed in the catalysts. In these peaks u^o (901.48 eV), and v^o (883.29 eV) are ascribed to Ce^{3+} ions XPS peaks, while u^i (907.78 eV), u^{ii} (917.18 eV), v^i (888.88 eV) and v^{ii} (897.88 eV) are ascribed to Ce^{4+} ions species.[31] De-convoluted split peaks confirm the presence of Ce^{3+} and Ce^{4+} ions in the CeO_2 oxides. The proportion of lattice oxygen and surface ion contents of Ce^{3+} had a significant effect on the performance of the catalyst. The percentage evaluation of Ce^{3+} state is calculated by Equation (1),

$$Ce^{3+}\ \% = \left(\frac{Ce^{3+}}{Ce^{3+} + Ce^{4+}}\right) \times 100 \quad (1)$$

Table 3 shows that Mn_2O_3/CeO_2–NP had the highest Ce^{3+} concentration among all particle-base catalysts.

Table 2. BET data of CeO_2 supports and Mn_2O_3/CeO_2 catalyst.

Sample	S_{BET} (m^2/g)	V_{total} (cm^3/g)	Pore size (nm)
CeO_2–NP	18.358	0.110	8.99
CeO_2–NC	17.021	0.099	9.25
CeO_2–NR	15.50	0.083	9.87
Mn_2O_3/CeO_2–NP	34.53	0.290	5.73
Mn_2O_3/CeO_2–NC	30.45	0.211	6.51
Mn_2O_3/CeO_2–NR	22.69	0.126	8.76

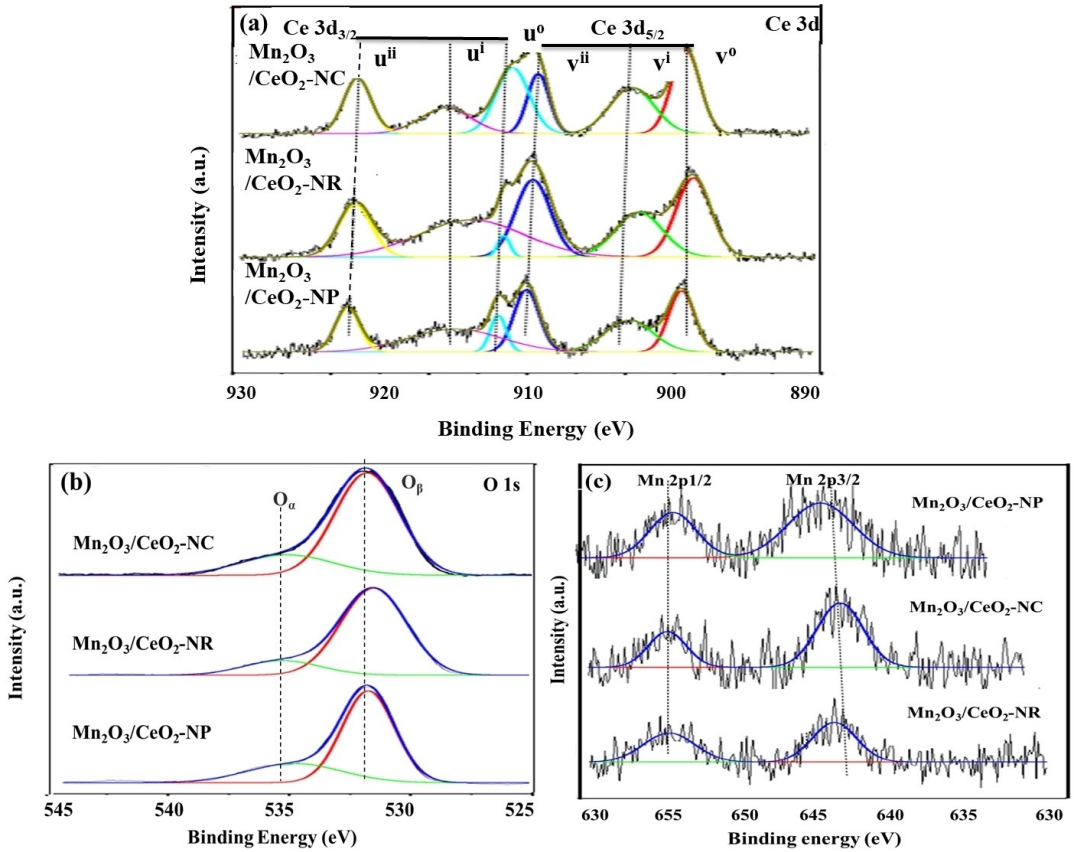

Figure 2. XPS spectra of (a) Ce 3d, (b) O 1s, and (c) Mn 2p catalysts.

Table 3. Atomic ratios of the catalysts by XPS spectra.

Catalysts	$(\frac{Ce^{3+}}{Ce^{3+}+Ce^{4+}})$	$(\frac{O_\alpha}{O_\alpha+O_\beta})$	$(\frac{Mn^{4+}}{Mn^{4+}+Mn^{3+}})$
Mn_2O_3/CeO_2–NR	0.3896	0.7022	0.7156
Mn_2O_3/CeO_2–NP	0.4353	0.7331	0.7621
Mn_2O_3/CeO_2–NC	0.4102	0.7276	0.7431

The de-convoluted O 1s spectra of Mn_2O_3/CeO_2 catalysts show two peaks marked as O_α and O_β, respectively, as shown in Figure 2(b). The first one is caused by lattice oxygen species, whereas second is caused by chemisorbed oxygen.[16,17,31] It is widely known that chemisorbed adsorb oxygen on defective catalyst sites has a high migratory potential, which helps in oxidization.[7,8] The relative concentration of O_α $(O_\alpha/(O_\alpha+O_\beta)$ is calculated, and are shown in Table 3. The Oxygen content of Mn_2O_3/CeO_2 catalysts is ranked as: Mn_2O_3/CeO_2–NP > Mn_2O_3/CeO_2–NC > Mn_2O_3/CeO_2–NR. It is implying that Mn_2O_3/CeO_2–NR has the more chemisorbed oxygen species.

As seen in Figure 2(c), the Mn 2p region consists of two peaks, Mn 2p3/2 with binding energy (BE) of approximately 643.7 eV and Mn2p1/2 with a binding energy of about 655.3 eV which are made up of Mn^{4+} and Mn^{3+}, indicating that Mn is in the mixed-valence state that is in Mn^{3+} and Mn^{4+} form.[31,32] For three catalysts, the $Mn^{3+}/(Mn^{3+}+Mn^{4+})$ content ratio is calculated and found that Mn_2O_3/CeO_2–NP has highest Mn^{4+} contents. The Mn^{4+} is catalyst's primary valence that play substantial role in the reduction reaction.[32]

SEM-EDX

The SEM and EDX images of CeO_2–NR, CeO_2–NC, and CeO_2–NP and catalysts: Mn_2O_3/CeO_2–NR, Mn_2O_3/CeO_2–NP, and Mn_2O_3/CeO_2–NC synthesized by the wet-impregnation method shown in Figure 3. The Figure 3(a), (d), and (g) are for CeO_2–NR, CeO_2–NC, and CeO_2–NP supports, and the Figure 3(b), (e), and (h) are for Mn_2O_3/CeO_2–NR, Mn_2O_3/CeO_2–NP, and Mn_2O_3/CeO_2–NC catalysts, while the EDX is in Figure 3(c), (f), and (i) respectively. Comparing the SEM images of all catalysts and their supports, it is clear that Mn_2O_3 is impregnated over the supports and also confirmed in EDX. Figure 3(c), (f), and (i). Comparing Figure 3(b), (e), and (h), it can be found that impregnation of Mn_2O_3 over CeO_2–NP made the morphology of CeO_2–NP more homogeneous and thus showing the high dispersion of active components (Mn_2O_3) over the surface of CeO_2–NP. It is also observed that the Mn_2O_3/CeO_2–NP shows less cluster formation compare to the Mn_2O_3/CeO_2–NC and Mn_2O_3/CeO_2–NR. The surface got less cluster, which means increasing the catalyst's specific surface area and providing additional reaction sites. The BET and XRD data also confirmed that Mn_2O_3/CeO_2–NP has a high surface area and low crystal size.

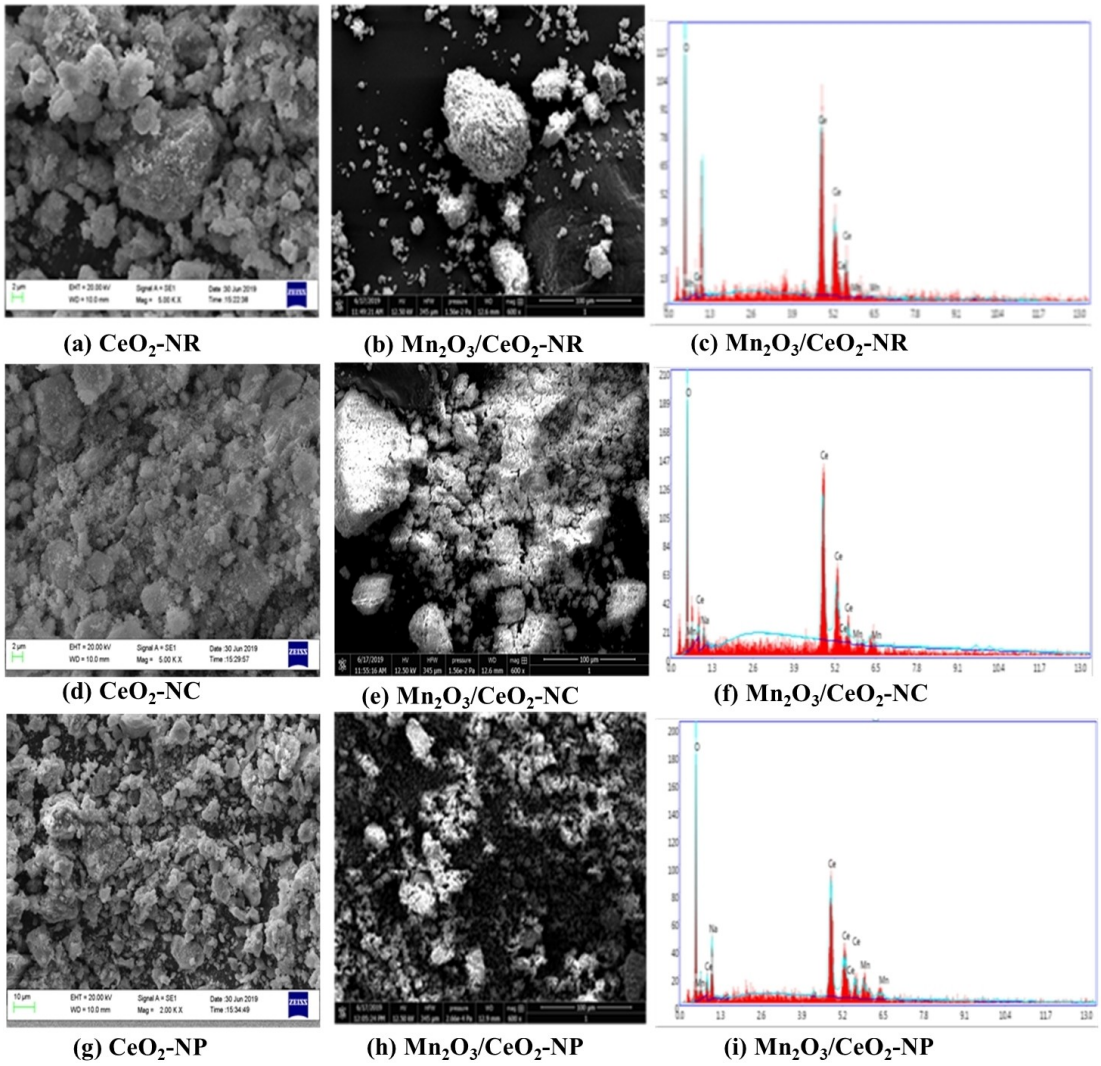

Figure 3. SEM and EDX images of CeO_2 supports and Mn_2O_3/CeO_2 catalysts.

TEM

TEM characterization was used to analyze the morphology structures and average particle size of synthesized CeO_2–NR, CeO_2–NP, and CeO_2–NC and Mn_2O_3/CeO_2–NR, Mn_2O_3/CeO_2–NP, and Mn_2O_3/CeO_2–NC catalysts. Figure 4 showed that the hydrothermal approach successfully synthesized CeO_2 supported morphologies such as CeO_2–NR, CeO_2–NC, and CeO_2–NP. The CeO_2–NP showing the smallest particle size compared to the other two supports. Figure 4(d), (e), and (f) showed that after impregnating Mn_2O_3 over CeO_2, all supports kept their original morphologies and followed the same particle size pattern that the supports followed. The textural parameters of all catalysts are shown in Table 1. The Mn_2O_3/CeO_2–NP sample had the smallest average particle size and the highest surface area out of the three catalysts, potentially beneficial for the NH_3–SCR reaction, followed by Mn_2O_3/CeO_2–NR and Mn_2O_3/CeO_2–NC. The particle size of Mn_2O_3/ CeO_2–NP is the highest, while the specific surface area is the smallest; it shows a correlation of BET surface area with TEM particle size data.

H_2-TPR

Figure 5 shows the H_2-TPR patterns of the supports and Mn_2O_3-based catalysts. CeO_2–NR showing a slightly higher reduction temperature (360 °C and 450 °C) compared to CeO_2–NP (298 °C and 400 °C) and CeO_2–NC (295 °C and 402 °C). It is related to the reduction of surface Ce^{4+} to Ce^{3+}. At low temperatures, CeO_2–NR had weaker reduction peaks than CeO_2–NC and CeO_2–NP, indicating weaker redox capability. It shows that the atoms in CeO_2–NR are arranged more strongly than the cube and particle state of CeO_2, showing more peaks area and hence more hydrogen consumption in reduction.[14] The reduction peaks at low temperature shifted to higher temperature after the impregnation of 10 wt.% Mn_2O_3 over ceria's morphology-based support.

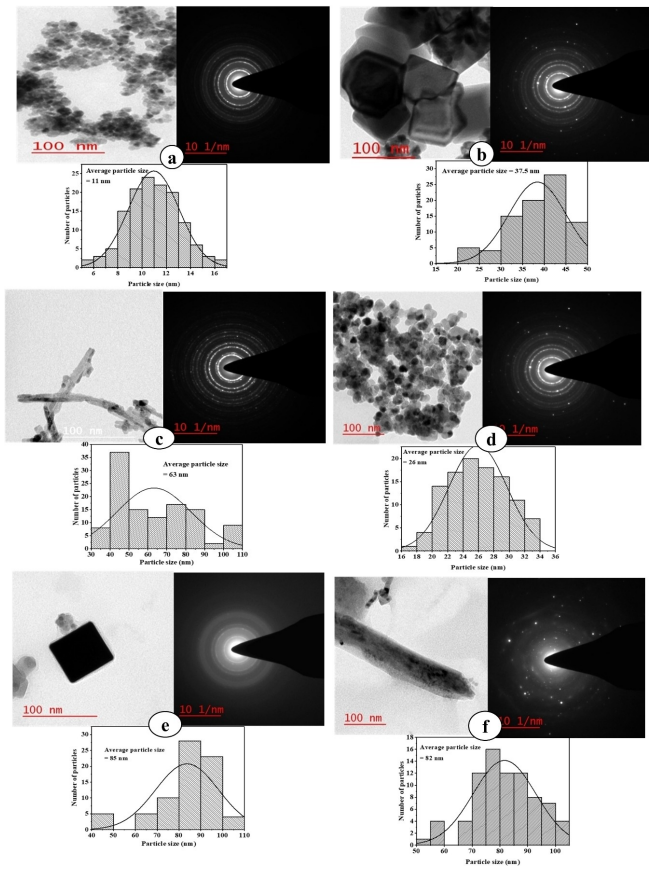

Figure 4. TEM images of supports,and catalysts (a) CeO_2–NP, (b) CeO_2–NC, (c) CeO_2–NR, (d) Mn_2O_3/CeO_2–NP, (e), Mn_2O_3/CeO_2–NC, (f) Mn_2O_3/CeO_2–NR.

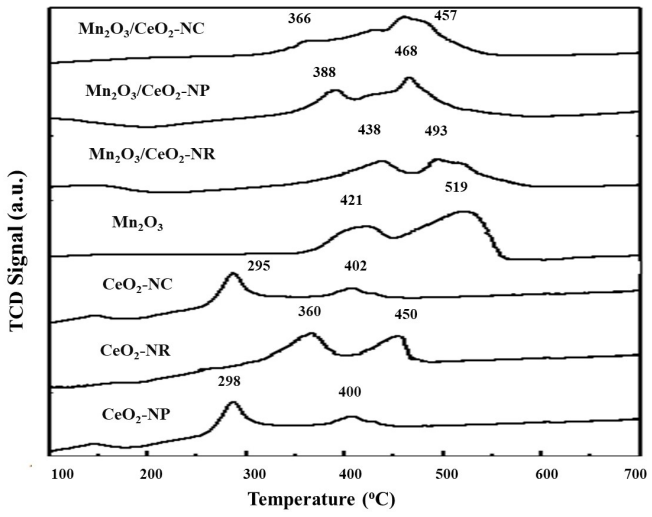

Figure 5. H_2-TPR profile Mn_2O_3, CeO_2–NR, Mn_2O_3/CeO_2–NR, CeO_2–NC, Mn_2O_3/CeO_2–NC, CeO_2–NP, Mn_2O_3/CeO_2–NP.

The Mn_2O_3 state shows two reduction peaks at 421 °C and 519 °C, and both are higher than Ceria supports with broader peaks. After loading Mn_2O_3 over CeO_2 based on different morphology, it showed a higher reduction temperature due to the synergetic effect of Mn_2O_3 with CeO_2. It shifted the reduction performance of the catalyst over 350 °C, broadening the range.

Catalytic Performance

NO catalytic activity

The NO conversions and N_2 selectivity of CeO_2 morphology (NP, NR, and NC) and Mn_2O_3 supported over different CeO_2 morphology catalysts in the temperature range of 50–450 °C are shown in Figure 6 and Figure 7.

The NO conversion and N_2 selectivity of ceria support are shown in Figure 6(a) and Figure 6(b), respectively. The highest conversion is 55 % for CeO_2–NP at 250 °C, followed by CeO_2–NC (40 %) and CeO_2–NR (27 %). The CeO_2–NP selectivity is slightly higher than others at low temperatures till 220 °C; however, CeO_2–NC and CeO_2–NR have shown the same selectivity throughout the process. The N_2 selectivity of all supports is nearly the same, reaching 76 % at 250 °C. After 250 °C, selectivity slightly declined, but the CeO_2–NP selectivity is still higher than the CeO_2–NC and CeO_2–NR. Table 2 shows that the CeO_2–NP has the highest specific surface area (18.358 m^2/g) and pore volume (0.110 cm^3/g) compared to CeO_2–NC and CeO_2–NR due to its lowest crystal size (Table 1, Figure 1), and abundant mesoporosity. All these reasons are behind the excellent performance of CeO_2–NP.

The NO conversion over Mn_2O_3 catalyst supported over different CeO_2 morphology is shown in Figure 7(a). All the catalysts showed better NO conversion in the temperature range of 300–450 °C. The NO conversion pattern is the same as the ceria supports; however, the temperature range increased after Mn_2O_3 loading on the supports, confirmed by H_2-TPR results. The Mn_2O_3/CeO_2–NP catalyst showed the highest NO conversion compared to NC and NR-supported catalysts. The activity order of NO conversion is as follows: Mn_2O_3/CeO_2–NP > Mn_2O_3/CeO_2–NC > Mn_2O_3/CeO_2–NR. The NO conversion pattern is the same as the ceria supports; however, the temperature range increased after Mn_2O_3 loading on the supports. The Mn_2O_3/CeO_2–NP catalyst exhibited 76 % NO conversion at 350 °C, higher than Mn_2O_3/CeO_2–NR and Mn_2O_3/CeO_2–NC due to the CeO_2–NP support provided high surface area, less cluster formation and showing a solid interaction between the Mn_2O_3 and CeO_2–NP. It has produced the highest Ce^{3+} (43.53 %), lattice oxygen (O_α = 73.31 %), Mn_2O_3 species dispersion (Mn^{4+} = 76.21 %), and more surface defects. Due to these catalysts' surface properties, Mn_2O_3/CeO_2–NP showed excellent NH_3–SCR performance. Other parameters such as high specific surface area (34.53 m^2/g), pore-volume (0.290 cm^3/g), and abundant mesoporosity also strongly affected the reduction reaction.

The N_2 selectivity profile of the catalysts, as depicted in Figure 7(b) clearly showed that the N_2 selectivity of the catalysts follows the same order as their NO conversion activity. At lower temperatures, the catalysts exhibited lower activity as well as selectivity.

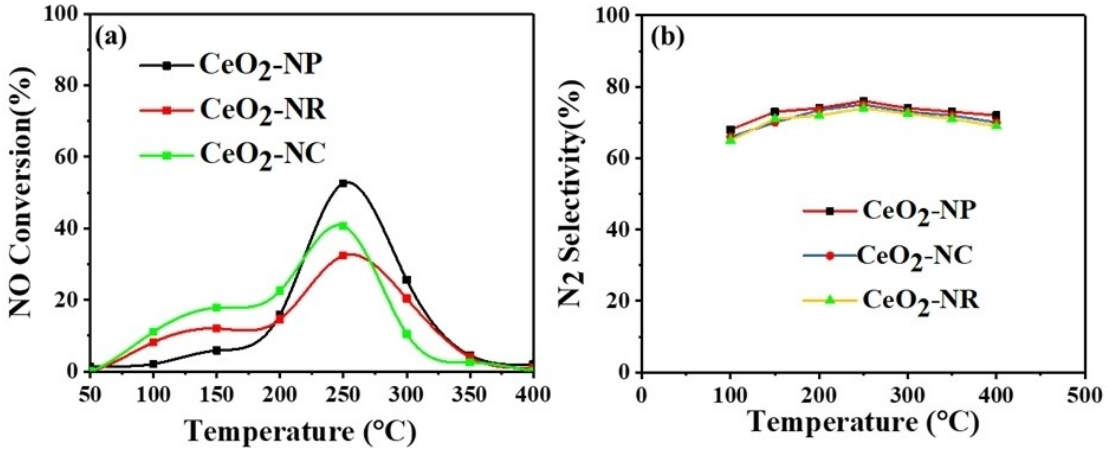

Figure 6. NO conversion and N_2 selectivity for CeO_2 supports. Reaction conditions: temperature range 50 to 450 °C, NO, NH_3 = 1000 ppm, O_2 = 6 vol %, Ar balance, and GHSV = 13,000 h^{-1}.

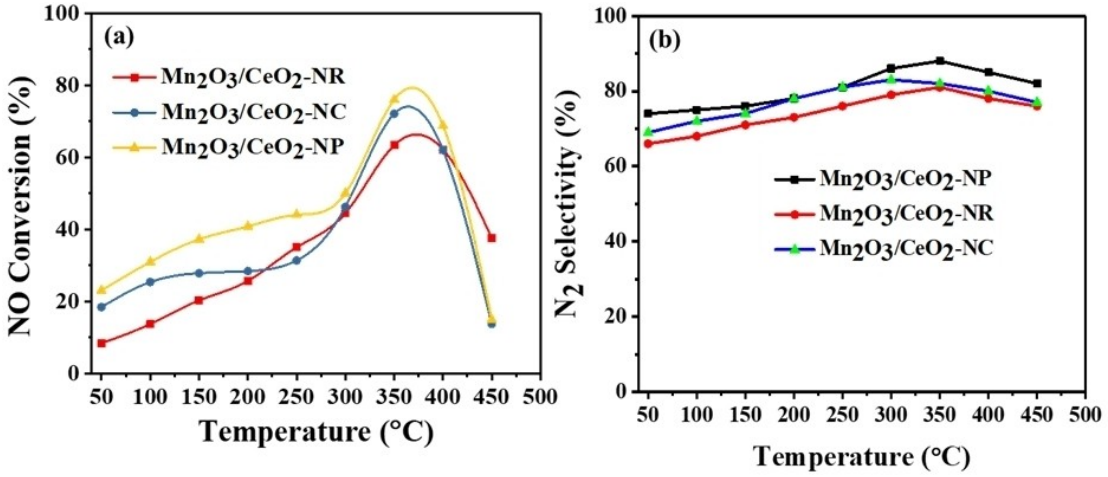

Figure 7. NO conversion and N_2 selectivity for catalysts. Reaction conditions: temperature range 50 to 450 °C, NO, NH_3 = 1000 ppm, O_2 = 6 vol %, Ar balance, and GHSV = 13,000 h^{-1}.

Effect of Mn_2O_3 loading on NH_3–SCR performance

In order to optimize the metal loading, different wt.% of Mn_2O_3(5, 10, and 15 wt.%) supported on CeO_2–NP catalysts were tested, and the results are shown in Figure 8. The 10 wt.% Mn_2O_3/ CeO_2–NP shows the highest NO conversion activity (Figure 8(a)) and N_2 selectivity (Figure 8(b)) of 78 % and 84 %, respectively at 350 °C. It may be due to the high active surface area and pore volume exhibited by 10 wt.% Mn_2O_3/ CeO_2–NP, which enhances the NO reduction to N_2. It is also observed that 10 wt.% Mn_2O_3 loading uplift the NO conversion ~ 80 % in the temperature range of 250 to 350 °C, as shown in Figure 8(a), further increasing the loading from 10 to 15 wt. %, the NO conversion decreased ~ 45 % may be due to agglomeration of active metal of Mn_2O_3 over CeO_2–NP. The low NO conversion exhibited by Mn_2O_3/CeO_2–NP at 5 wt.% loading was probably due to insufficient Mn_2O_3 loading amount leading to fewer active sites and less synergism between Mn_2O_3 and CeO_2–NP. In case of higher loading of 15 wt.%, besides unoptimized synergism between Mn_2O_3 and CeO_2–NP, the high agglomeration or cluster formation by Mn_2O_3, as evident by the decrease in its surface area, could be the reason behind its low NO conversion activity. However, when it comes to N_2 selectivity, the 15 wt.% Mn_2O_3/CeO_2–NP shows a higher N_2 selectivity than 5 and 10 wt.% Mn_2O_3 loading over CeO_2–NP. There is no clear information about this, but it can be concluded that the N_2 selectivity is independent of catalyst surface area and pore volume and most probably dependent on other physicochemical properties of catalysts.

Characterization results of used catalysts

The XRD pattern of all used CeO_2 supports, and Mn_2O_3 supported catalysts are shown in Figure 9. The XRD pattern (shown in Figure 1) revealed an insignificant effect on the diffraction pattern, but there is an increase in sharpness in

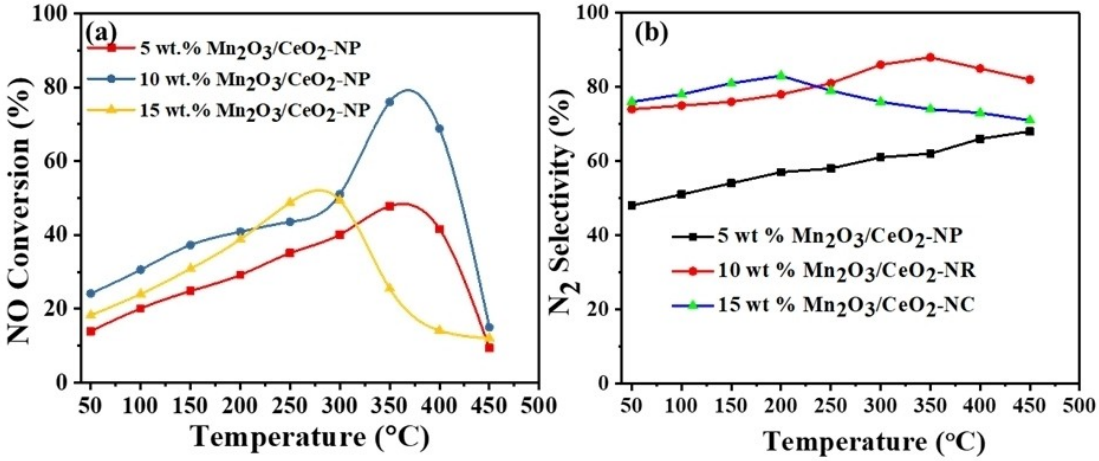

Figure 8. NO conversion and N_2 selectivity for wt. % of Mn_2O_3 on CeO_2–NP. Reaction conditions: temperature range 50 to 450 °C, NO, NH_3 = 1000 ppm, O_2 = 6 vol %, Ar balance, and GHSV = 13,000 h^{-1}.

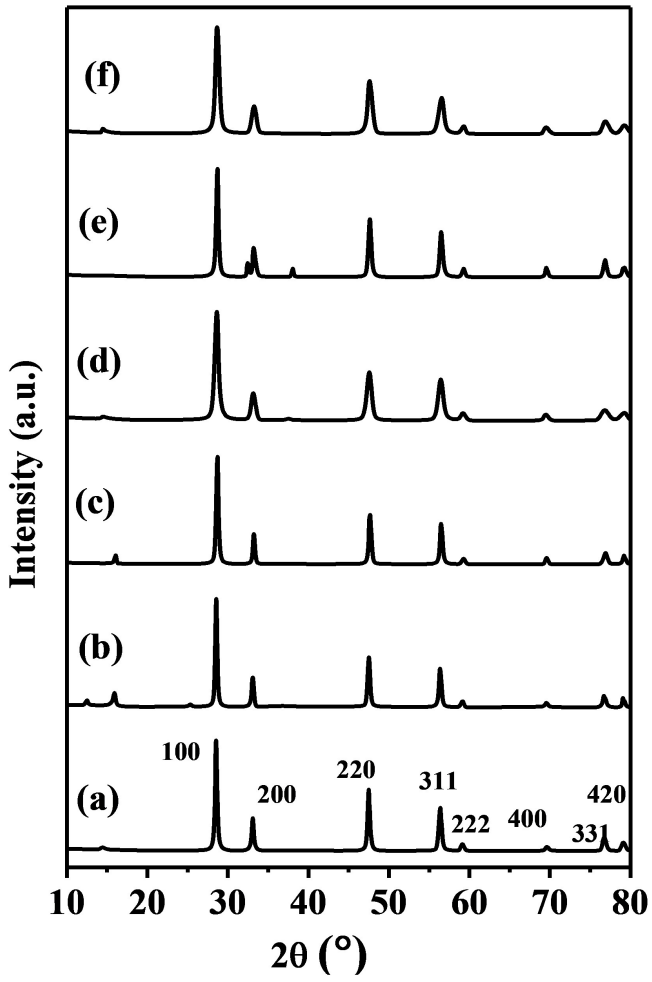

Figure 9. XRD of (a) used CeO_2–NP, (b) used CeO_2–NC, (c) used CeO_2–NR, (d) used Mn_2O_3/ CeO_2–NP, (e) used Mn_2O_3/ CeO_2–NC,and (f) used Mn_2O_3/ CeO_2–NR.

peaks. There is also an increase in the crystal size of both supports and catalysts, shown in Table 4, and it may be due to cluster formation at high temperatures.

TEM images of used catalysts are shown in Figure 10. Comparing Figure 4 with Figure 10 exhibited the same morphology, which means the effects of high temperature didn't affect the catalysts' morphology properties but increased the particles' size, which may be due to cluster formation.

Conclusions

The effect of morphology and support interaction on CeO_2 (NP, NC, NR) and Mn_2O_3/CeO_2 catalysts for NH_3–SCR of NO has been studied thoroughly. The Mn_2O_3/CeO_2–NP catalyst synthesized from CeO_2–NP had the highest catalytic performance among the Mn_2O_3/CeO_2–NR, Mn_2O_3/CeO_2–NP, and Mn_2O_3/CeO_2–NC catalysts, with around 76% NO conversion and 85% N_2 selectivity at 350 °C. The temperature increases in a wide range after the Mn_2O_3 loading on the supports. The highest catalytic performance of Mn_2O_3/CeO_2–NP could be attributed to its low crystal size (8.3 nm) and the highest specific surface area (34.53 m^2/gm), facilitating better Mn_2O_3 species dispersion (Mn^{4+} = 76.21 %) and more surface defects. As a result, Mn_2O_3/ CeO_2–NP has a higher surface oxygen content (73.31 %) and a better redox capacity. The stability of the catalysts is excellent; from the used catalysts data, it is clear that the XRD pattern and morphology were not affected too much throughout the process, only slightly changing in crystal size and particles size due to cluster formation at high temperature.

Supporting Information Summary

The experimental procedure, which includes materials and methods, catalyst preparation, characterization, and catalytic performance, is described in this section.

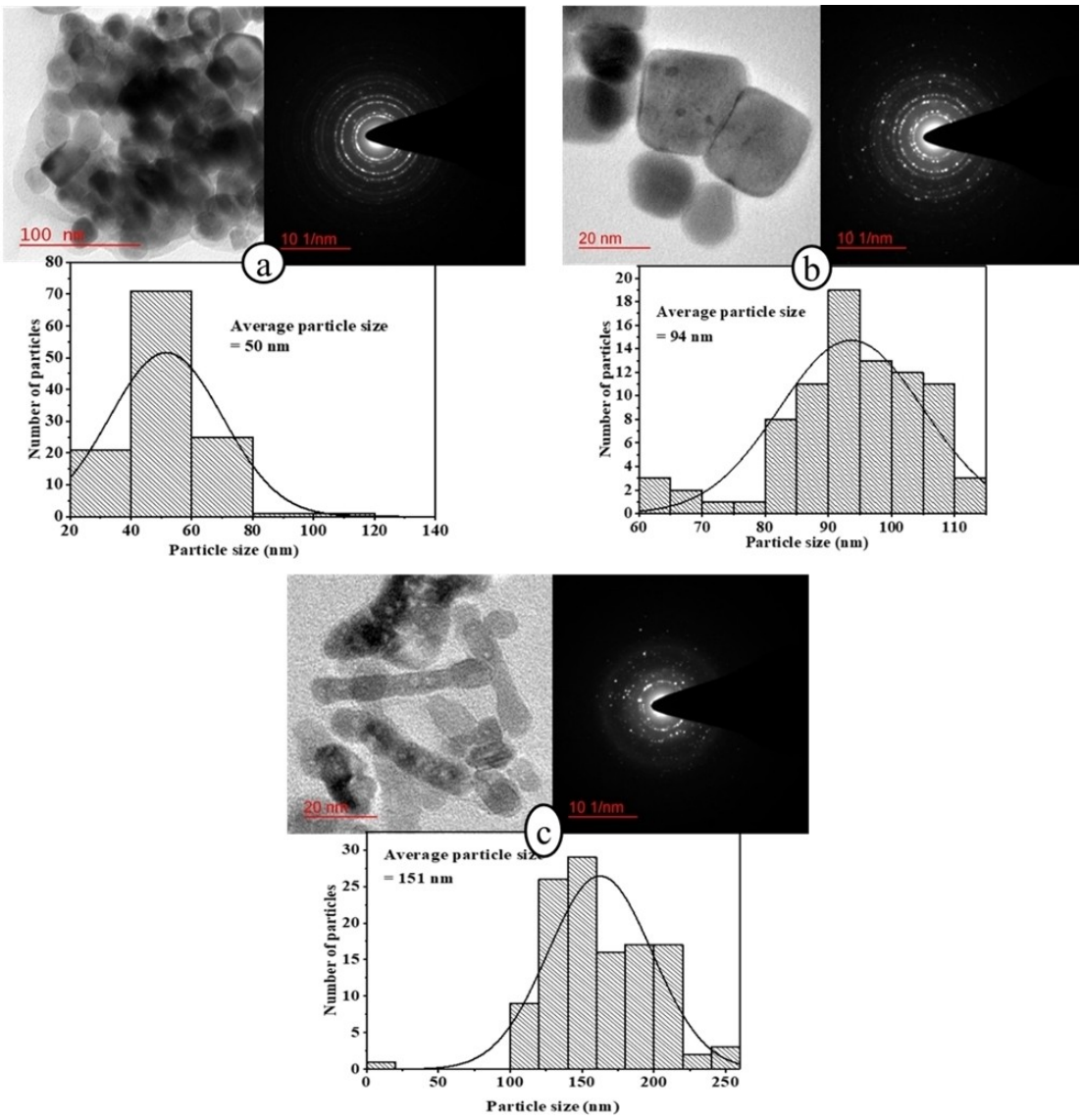

Figure 10. TEM images of (a) used Mn_2O_3/CeO_2 –NP, (b) used Mn_2O_3/CeO_2–NC, and (c) used Mn_2O_3/CeO_2–NR.

Table 4. Crystal size of used samples.

Sample	Crystal size (nm)	Average particle size (nm)
CeO_2–NP	8.6	–
CeO_2–NC	13	–
CeO_2–NR	13.5	–
Mn_2O_3/CeO_2–NP	10	50
Mn_2O_3/CeO_2–NC	14	94
Mn_2O_3/CeO_2–NR	10	151

Acknowledgements

The authors acknowledge the financial support, instrumentation, and characterization facilities provided by the Indian Institute of Technology (Banaras Hindu University), Varanasi, even though this research received no specific financing from the public, commercial, or non-profit funding bodies.

Conflict of Interest

The authors declare no conflict of interest.

Data Availability Statement

Research data are not shared.

Keywords: CeO_2-morpholgy · catalysis · heterogeneous · Mn_2O_3 · NH_3–SCR

[1] J. Chen, P. Fu, D. Lv, Y. Chen, M. Fan, J. Wu, A. Meshram, Mu B, Li X, Xia Q, *Chem. Eng. J.* **2021**, 407, 127071.
[2] X. Yao, L. Chen, J. Cao, F. Yang, W. Tan, L. Dong, *Ind. Eng. Chem. Res.* **2018**, 57, 12407–12419.
[3] F. Gao, C. Yang, X. Tang, H. Yi, C. Wang, *Res. J. Environ. Sci.* **2022**, 113, 204–218.

[4] Y. Jiang, T. Liu, W. Gao, H. Ge, Z. Yang, R. Lin, X. Wang, *Chem. Eng. J.* **2022**, 134576.
[5] Yang, Y. Fu, Y. Liao, S. Xiong, Z. Qu, N. Yan, J. Li, *Catal. Sci. Technol.* **2014**, 4, 224–232.
[6] Z. Han, X. Li, X. Wang, Y. Gao, S. Yang, L. Song, *J. Colloid Interface Sci.* **2022**, 606, 21445–1456.
[7] F. Gao, X. Tang, S. Zaharaddeen, H. Yi, S. Zhao, Q. Yu, Y. Shi, Y. Zhou, S. Ni, *Catal. Sci. Technol.* **2020**, 10, 7486.
[8] X. Xiao, S. B. Xiong, Y. Li, S. Geng, Yang, *Catal. Lett.* **2016**, 146, 2242–2251.
[9] Y. Ye, Z. Zang, T. Zhou, F. Dong, S. Lu, X. Tang, W. Wei, Y. Zhang, *J. Catal.* **2018**, 357, 100–107.
[10] Z. Lian, W. Shan, Y. Zhang, M. Wang, H. He, *Ind. Eng. Chem. Res.* **2018**, 57, 12736–12741.
[11] X. Chen, X. S. Cao, X. Weng, H. Wang, Wu, *Catal. Commun*. **2012**, 26, 178–182.
[12] Y. Geng, W. Shan, F. Liu, S. Yang, *J. Hazard. Mater.* **2021**, 405, 124223.
[13] L. Yu, R. Peng, L. Chen, M. Fu, J. Wu, D. Ye, *Chem. Eng. J.* **2018**, 334, 2480–2487.
[14] X. Yo, L. Chen, J. Cao, F. Yang, W. Tan, L. Dong, *Ind. Eng. Chem. Res.* **2018**, 57, 12407–12419.
[15] D. Wang, Y. Peng, O. Yang, F. Hu, J. Li, J. Crittenden, *Catal. Today*. **2019**, 332, 42–48.
[16] H. Chang, J. Li, J. Yuan, L. Chen, Y. Dai, H. Arandiyan, J. Xu, J. Hao, *Catal. Today*. **2013**, 201, 139–144.
[17] S. Andreoli, F. A. Deorsola, R. Pirone, *Catal. Today*. **2015**, 253, 199–206.
[18] D. Wook, K. Won, K. B. Nam, S. C. Hong, *Appl. Catal. B.* **2015**, 166–167, 37–44.
[19] C. Tang, H. Zhang, L. Dong, *Catal. Sci. Technol.* **2016**, 6, 1248–1264.
[20] C. Liu, J–W. Shi, C. Gao, C. Niu, *APPL CATAL A-GEN.* **2016**, 522, 54–69.
[21] Y. Xiong, C. Tang, X. Yao, L. Zhang, L. Li, X. Wang, Y. Deng, F. Gao, L. Dong, *Appl. Catal. A* **2015**, 495, 206–216.
[22] X. Yao, K. Ma, W. Zou, S. He, J. An, F. Yang, L. Dong, *Chin. J. Catal.* **2017**, 38, 146–159.
[23] H. Chang, J. Li, X. Chen, L. Ma, Yang, Johannes, W. Schwank, J. Hao, *Catal. Commun.* **2012**, 27,54–57.
[24] Z. Liu, Y. Yi, S. Zhang, T. Zhu, J. Zhu, J. Wang, *Catal. Today.* **2013**, 216, 76–81.
[25] S. Lia, B. Huang, C. Yua, *Catal. Commun.* **2017**, 98, 47–51.
[26] L. Zhong, Q. Fang, X. Li, Q. Li, C. Zhang, G. Chen, *Appl. Catal. A* **2019**, 579, 151–158.
[27] C. Wang, F. Yu, M. Zhu, C. Tang, K. Zhang, D. Zhao, L. Dong, D. Dai, *Res. J. Environ. Sci.* **2019**,75, 124–135.
[28] C. Liu, G. Gao, J. Shi, C. He, G. Li, N. Bai, C. Niu, *Catal. Commun.* **2016**, 5, 36–40.
[29] L. Weiman, L. Haidi, C. Yunfa, *RSC Adv*. **2019**, 9, 11912.
[30] V. K. Patel, S. Sharma, *Catal. Today*. **2021**, 375, 591–600.
[31] W. Li, C. Zhang, X. Li, P. Tan, A. Zhou, Q. Fang, Q. Chen, *Chin. J. Catal.* **2018**, 39, 1653–1663.
[32] X. Chen, H. Abdullah, D. H. Kuol, *Sci. Rep*. **2017**, 7, 41194.

Submitted: January 24, 2022
Accepted: July 11, 2022